Supporting Information

Interfacial Electron Transfer of MOF-Derived Co-B-P catalyst for hydrogen evolution reaction with improved activity and stability

Qi Zhang,[a] Siyuan Xu,[a] Qunlong Wang,[a] Ruijing Wang,[a*] Guangfeng Wei,[a*] Xuefeng Wang [a*]

[a]Shanghai Key Lab of Chemical Assessment and Sustainability, School of Chemical Science and Engineering, Tongji University, 1239 Siping Rd., Shanghai, 200092, P. R. China. E-mail: xfwang@tongji.edu.cn

Table of Contents

Section S1. Experimental Procedures

1.1 Materials and Chemicals.

Cobalt nitrate hexahydrate ($Co(NO_3)_2{\cdot}6H_2O$, 99%), hydrochloride (HCl, 99%), sodium borohydride ($NaBH_4$, 99%), ethanol (C_2H_5OH, 99%) were obtained from Sinopharm Chemical Reagent, Shanghai. Urea (NH_2CONH_2, 98%), ammonium fluoride (NH_4F, 99%) were purchased from Chinasun Specialty Products. 2-Methylimidazole ($C_4H_6N_2$, 99%) was purchased from Macklin, Shanghai. Sodium hypophosphite ($NaPH_2O_2$, 99%), Sodium hydroxide (NaOH, 98%), potassium hydroxide (KOH, 99%), and 10 wt% Pt/C were purchased from Aladdin, Shanghai. Commercial nickel foam (NF) was purchased from Shanghai Metal Company. All the chemicals were used as received without further purification.

1.2 Synthesis of Catalysts.

Synthesis of CoO nanosheet (CoO NS):

First, 1.5 mmol $Co(NO_3)_2{\cdot}6H_2O$, 7.5 mmol urea, and 3 mmol NH_4F were dissolved in 50 mL of deionized water respectively, and stir the solution until the dissolution was clear. Second, the above solution, together with a piece of cleaned NF (2×3 cm^2), was loaded into a Teflon-lined stainless autoclave. The sealed autoclave was heated at 110 °C for 2.5 h and then cooled down to room temperature naturally. The NF-supported sample was washed with deionized water and ethanol, and dried under the oven. In the subsequent calcination treatment, the sample was heated up to 350 °C at a ramping rate of 1 °C min^{-1} in Ar atmosphere and then held at this temperature for 2 h.

Synthesis of ZIF-67 precursor:

4.926g of 2-MI was dissolved in 20 mL of deionized water, and the NF loaded with CoO nanosheets was immersed in the solution and allowed to react for 6 hours. After the reaction, the NF was removed, washed several times with deionized water and ethanol, and dried. The obtained sample was then annealed at 350 °C for 2 hours under Ar atmosphere with a heating rate of 1 °C min^{-1}.

Synthesis of Co-B hierarchical nanoarray (Co-B HNA):

Dissolve 40 mmol of $NaBH_4$ in 40 mL of 0.1 M NaOH with continuous stirring to obtain an alkaline $NaBH_4$ solution. Then the above ZIF-67 precursor was placed to the alkaline $NaBH_4$ solution. The reaction was proceeded at room temperature for 24 hours until no bubbles were produced. After the reaction the NF was taken out, and then washed with deionized water and ethanol. Finally, the NF was dried under the oven.

Synthesis of CoB/Co_2P hierarchical nanoarray (CoB/Co_2P HNA):

0.25 g of NaH_2PO_2 was placed at the upstream side of a porcelain boat, while the previously obtained NF sample was placed downstream of the porcelain boat. The system was then heated to 350 °C at a rate of 3 °C min^{-1} under an Ar atmosphere and maintained at that temperature for 2 hours. After the reaction, the NF sample was washed with deionized water and dried under the oven to obtain CoB/Co_2P HNA. The Co-B NS was directly subjected to the above boronization and phosphorization process to obtain the comparative catalyst, denoted as Co-B-P NS.

1.3 Characterizations.

The surface morphology of the catalyst was examined by field-emission scanning electron microscopy (FESEM, Hitachi S-4800, Japan) and transmission electron microscopy (TEM, JEOL JEM-2100, Japan). The structural characteristics were investigated using X-ray diffraction (XRD, Bruker D8 Advance diffractometer) with Cu Kα radiation (λ = 1.5406 Å). The surface elemental composition and electronic states were analyzed via X-ray photoelectron spectroscopy (XPS, Thermo Fisher Scientific) using an Al Kα X-ray source. The contents of CoB/Co_2P HNA were determined by ICP-OES (Agilent 5110, Agilent Technologies Inc). Raman spectra were collected using 532 nm wavelengths (Renishaw Invia). The in-situ Raman spectra were recorded via Raman spectroscopy (LabRam Odyssey) using 532 nm wavelengths.

1.4 Electrochemical characterization.

All electrochemical measurements were conducted in a 1 M KOH solution using the CHI 660D electrochemical workstation from Chenghua, Shanghai. The as-synthesized catalyst served as the working electrode. A saturated Ag/AgCl electrode and a graphite rod (99.9995% purity, Alfa Aesar) were served as the reference and counter electrode, respectively. The linear sweep voltammetry curve (LSV) was obtained at a scan rate of 5 mV s^{-1}. The electrochemical impedance spectroscopy (EIS) was used to determine the solution and charge transfer resistances, with frequencies ranging from 10 kHz down to 0.1 Hz at an amplitude of 5 mV. The electrochemically active surface area (ECSA) of the catalyst was calculated based on the double-layer capacitance (C_{dl}), which was measured by cyclic voltammetry (CV) in the non-Faradaic region. Cs is the specific capacitance of a flat, smooth electrode surface which was taken as 40 μF cm^{-2}. All potential values were converted to the reversible hydrogen electrode (RHE) scale using the equation: $E_{RHE} = E_{Ag/AgCl} + 0.197 + 0.059pH$. The Faradaic efficiency (FE) was calculated as: FE (%) $=2n_{H2}F/Q*100\%$. For the comparison, the Pt/C was used as reference in HER tests. All the data in the main text are without the iR correction.

Section S2. Calculation Methods

2.1 Computational Details.

The DFT calculations were finished by the VASP software[1] and the LASP software platform (Liu Z P. LASP History [DB/OL]. (2018) http://laspmol.lasphub.com/Intro_eng.asp.). The exchange-correlation effects of energy were achieved through generalized gradient approximation method using the PBE functional. The plane-wave cutoff energy was set to 450 eV. The Monkhorst–Pack k-point mesh with a maximum spacing of 0.05 Å was utilized for first Brillouin zone integrations. The models for CoB/Co_2P were created from the (100) plane of Co_2P bulk and the (100) plane of CoB bulk. The lattice parameters of CoB/Co_2P are 6.24 Å × 10.40 Å × 30.00 Å, with $\alpha = 90°$, $\beta = 90°$ and $\gamma = 90°$, of which the lattice mismatch on the 001 plane is 4.71% × 0.25%, indicating its stability is tolerable. The surface energy of the interface is 0.0015 eV/nm^2. In this model, the angle between CoB (021) and interface is about 90°, and the angle between Co_2P (121) and interface is about 50°, which conforms to the TEM results. The vacuum space is adopted more than 15 Å above the molecular to separate periodic interactions during the whole calculations. The Quasi-Newton l-BFGS method was used for geometry relaxation until the maximal force on each degree of freedom was less than 0.05 eV/Å.

Section S3. Supplementary Information

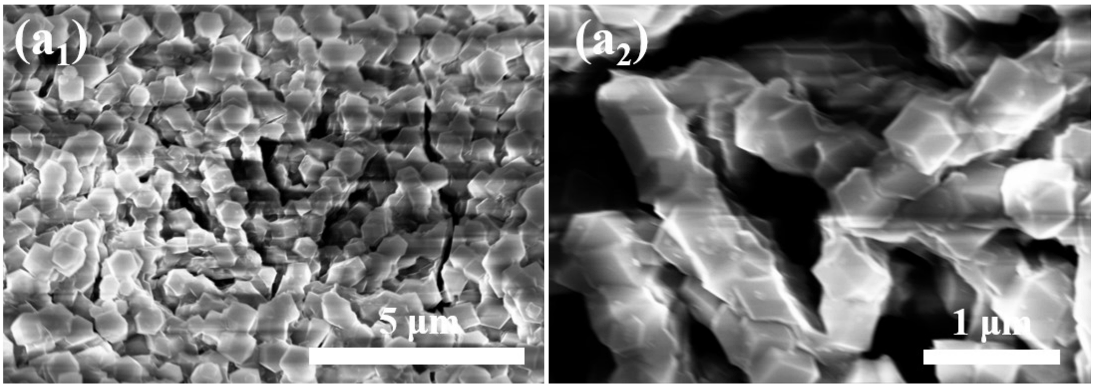

Figure S1. Low- and high-magnification SEM images of (a$_1$–a$_2$) ZIF-67 precursor.

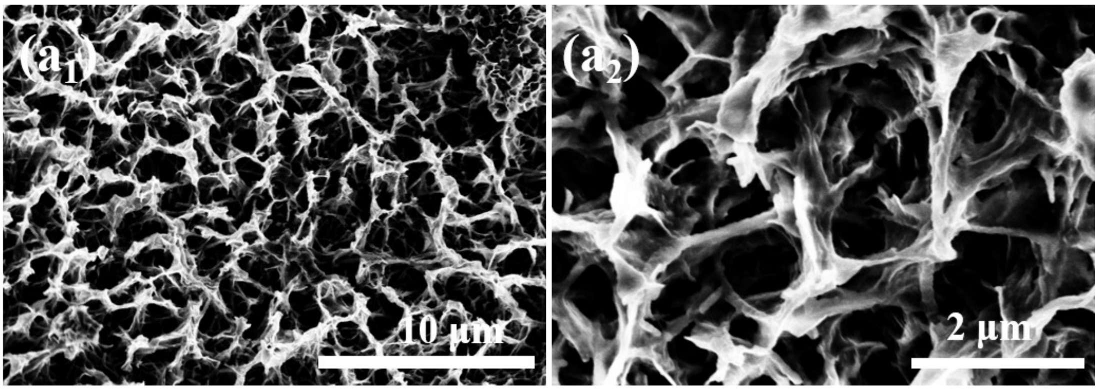

Figure S2. Low- and high-magnification SEM images of (a$_1$–a$_2$) Co-B-P NS.

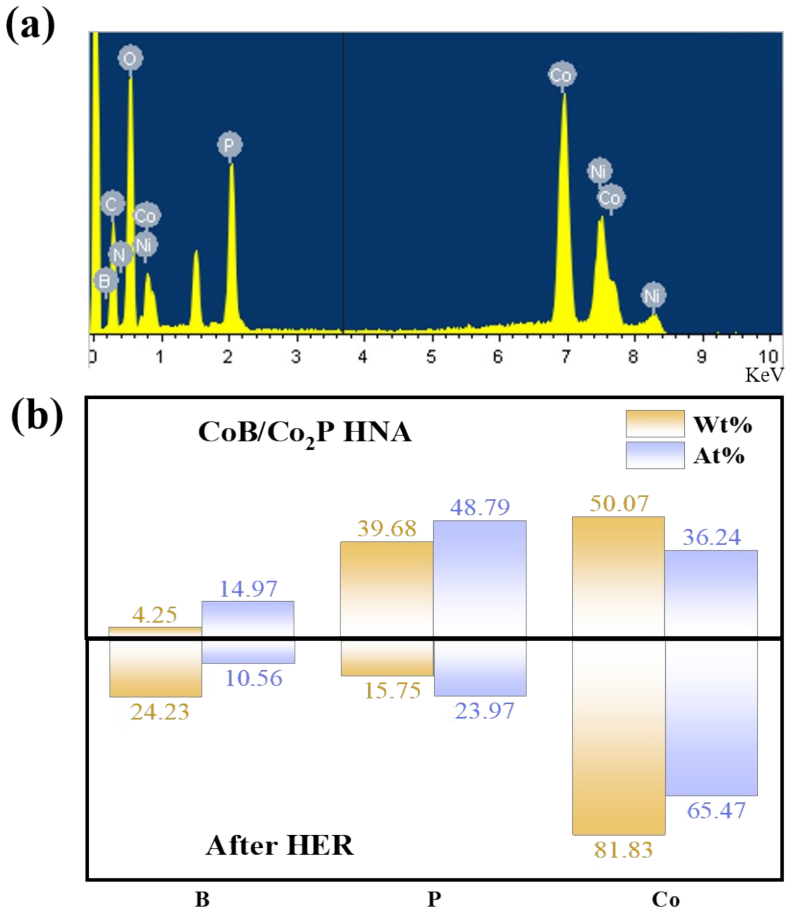

Figure S3. (a) EDS elemental images of CoB/Co$_2$P HNA, (b) Composition of CoB/Co$_2$P HNA and post-HER CoB/Co$_2$P HNA determined by the ICP-OES.

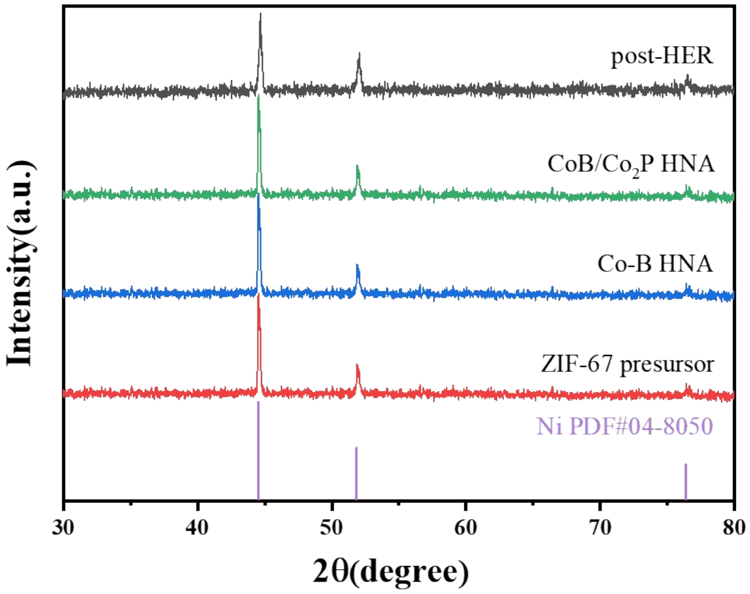

Figure S4. XRD patterns of ZIF67precursor, Co-B HNA, CoB/Co_2P HNA and post-HER CoB/Co_2P HNA.

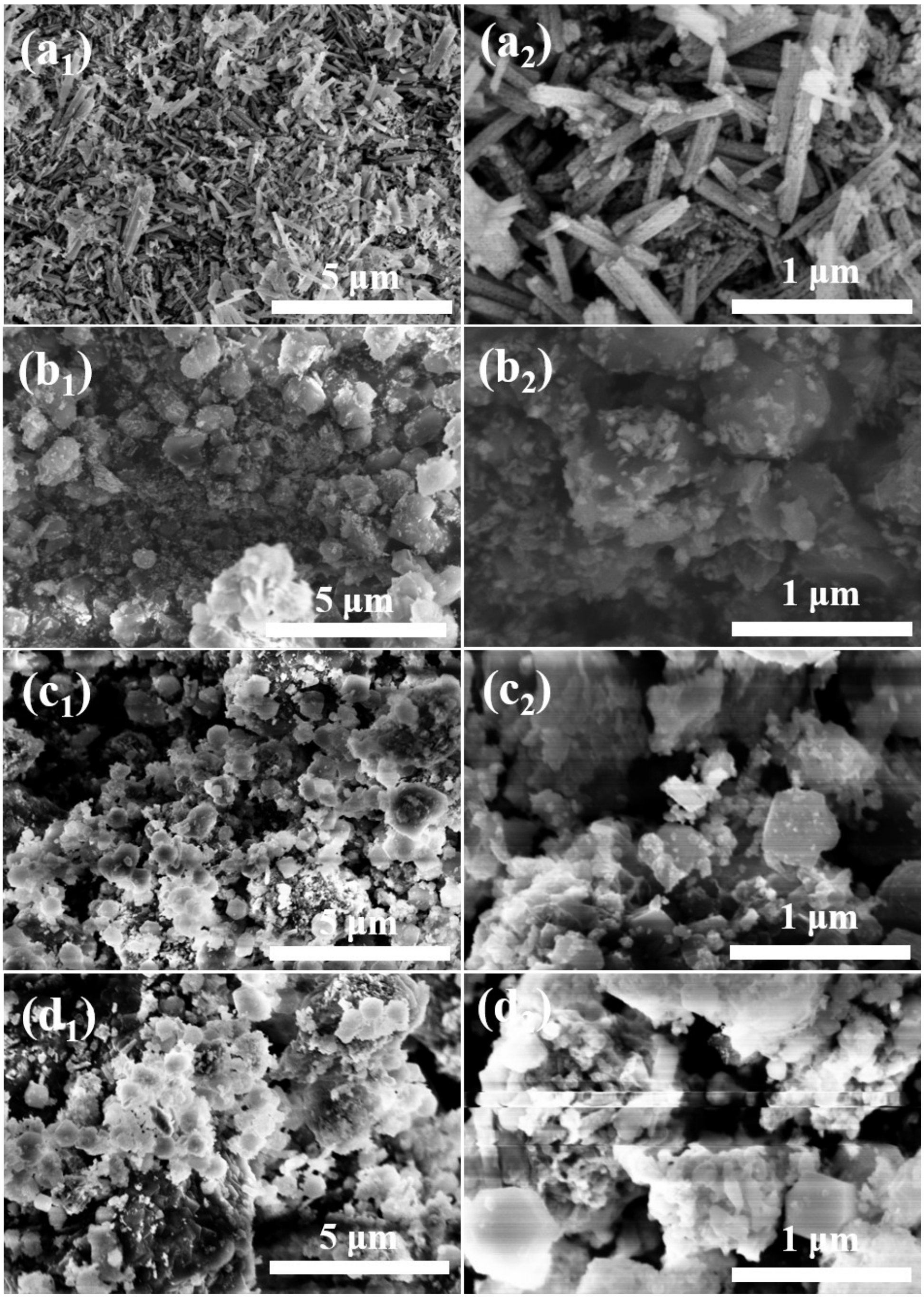

Figure S5. Low- and high-magnification SEM images of the powder form of (a_1–a_2) CoO, (b_1–b_2) ZIF-67 precursor, (c_1–c_2) Co-B, (d_1–d_2) CoB/Co_2P.

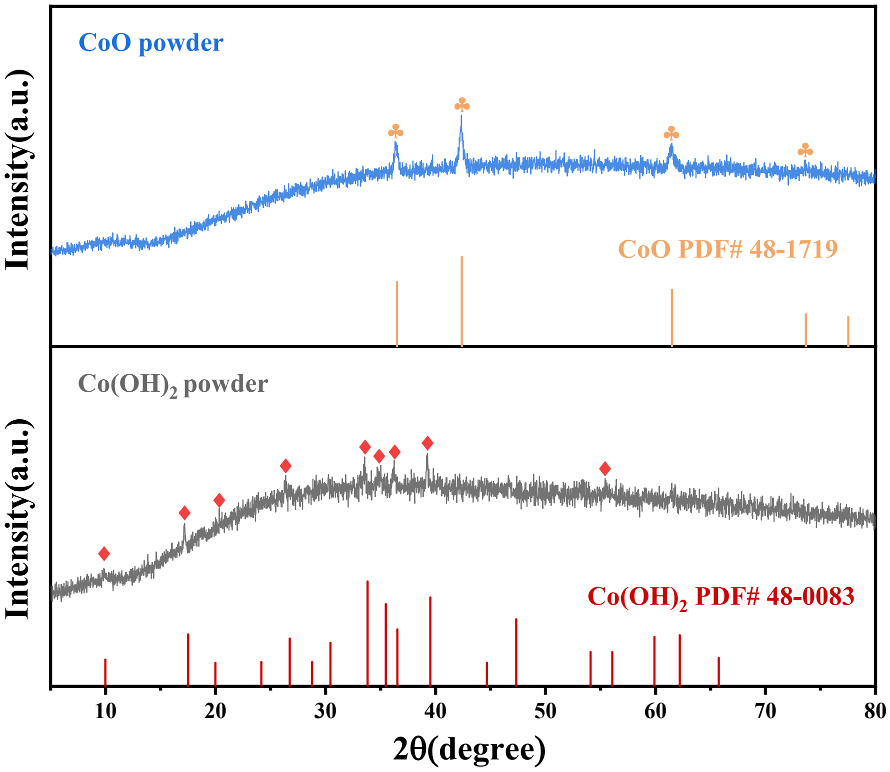

Figure S6. XRD patterns of the powder form of Co(OH)$_2$ and CoO.

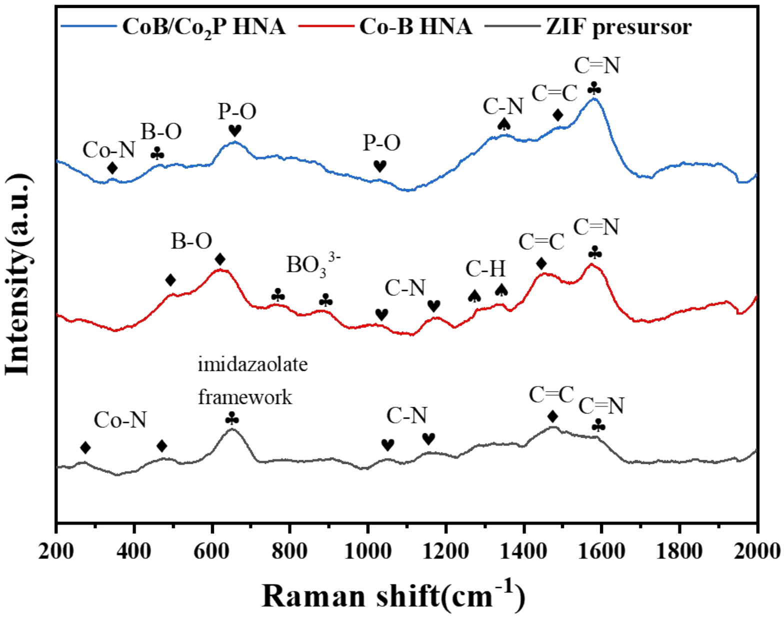

Figure S7. Raman spectra of ZIF67precursor, Co-B HNA, CoB/Co_2P HNA

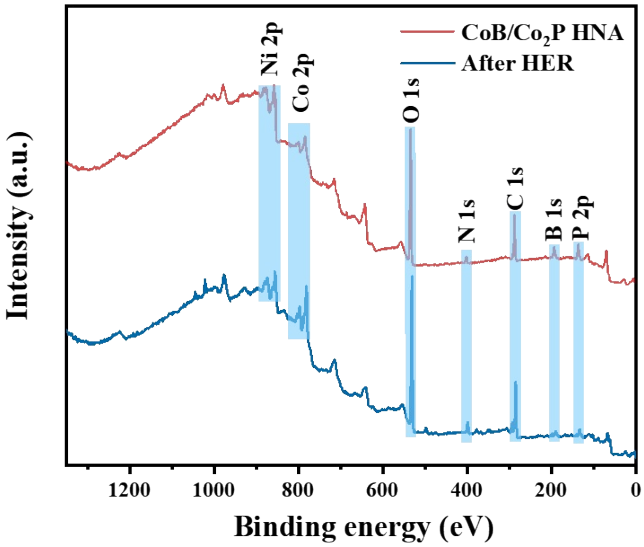

Figure S8. XPS survey-spectra of CoB/Co$_2$P HNA and post-HER CoB/Co$_2$P HNA.

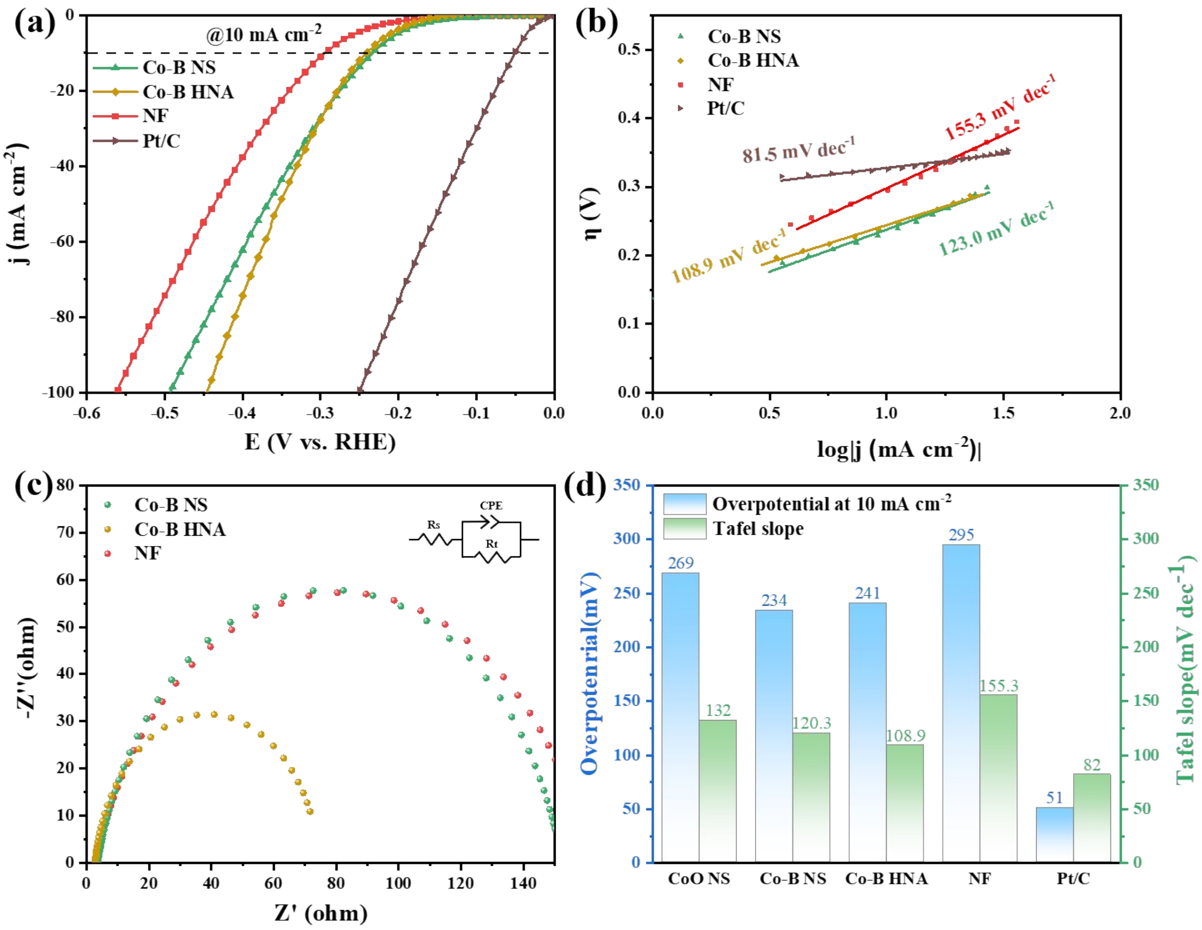

Figure S9. Evaluation for HER: (a) LSV curves (b) corresponding Tafel plots and (c) EIS Nyquist plots (d) Tafel plots and overpotential at 10 mA cm^{-2} comparisons of Co-B NS, Co-B HNA, NF and Pt/C.

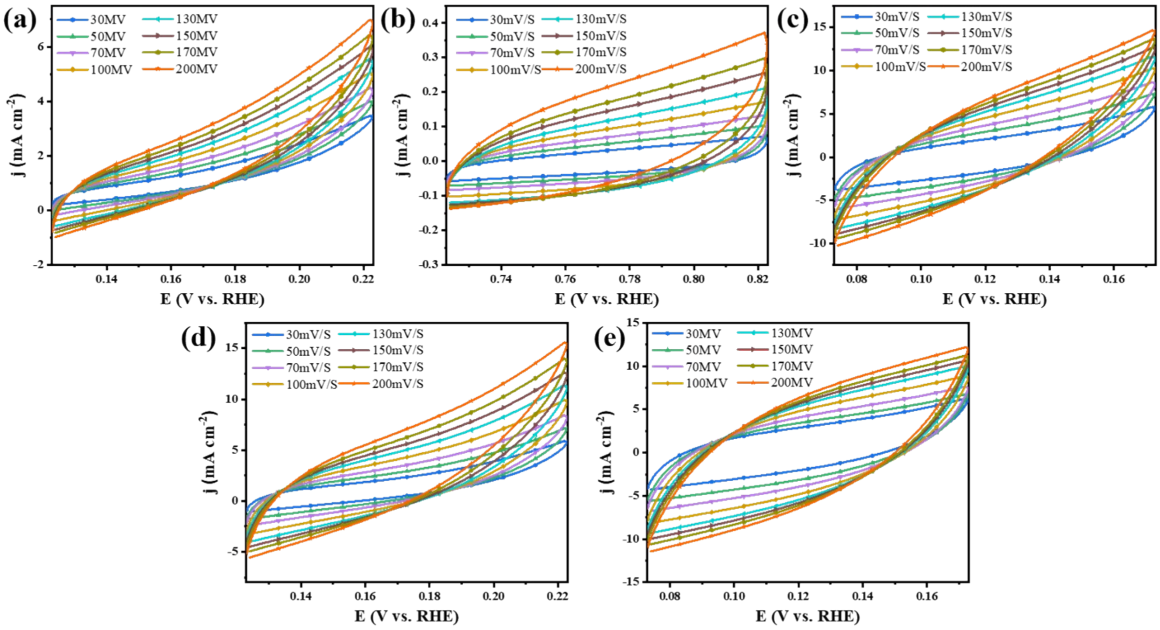

Figure S10. Cyclic voltammograms at different scan rates of 30, 50 70, 100,130,150,170 and 200 mV s^{-1} of (a) CoO NS, (b) Co-B NS, (c) Co-B-P NS, (d) Co-B HNA, and (e) CoB/Co$_2$P HNA. In the non-Faradaic region of these CV curves, the current response mainly arises from the charging and discharging of the electrochemical double layer, without noticeable redox peaks. This potential range is selected as the non-Faradaic region to evaluate the double-layer capacitance (C_{dl}), and the corresponding electrochemically active surface area (ECSA).

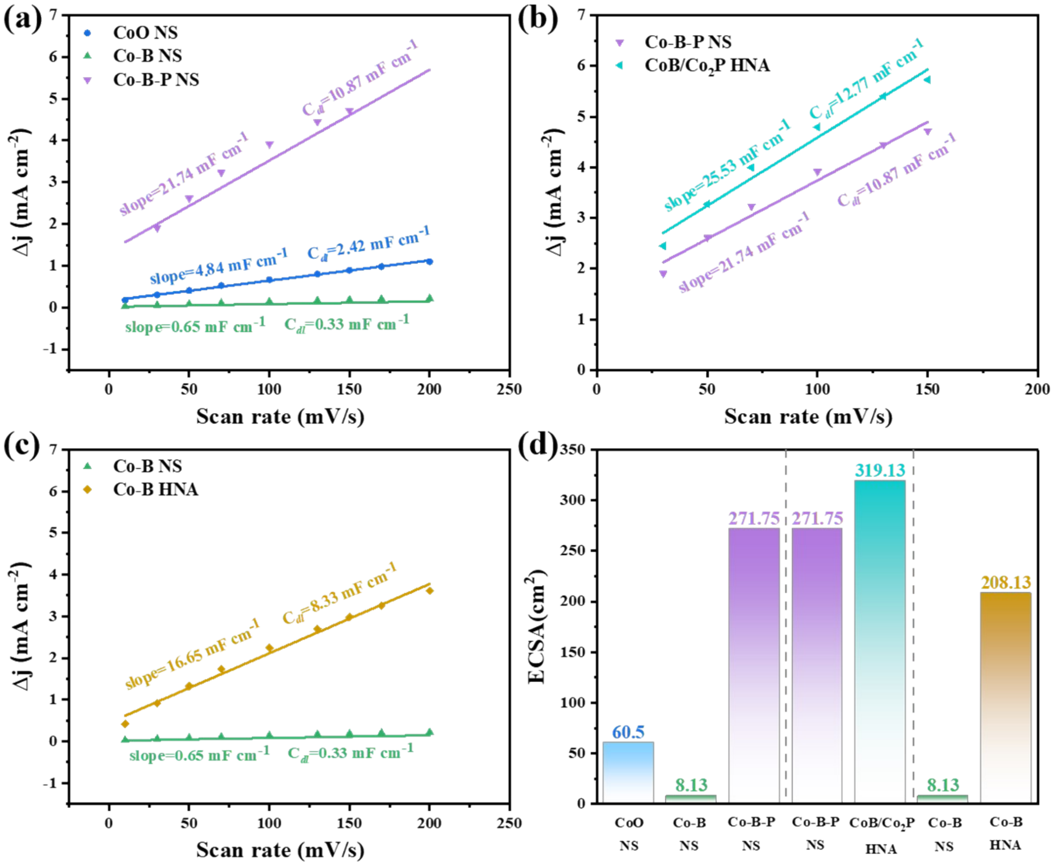

Figure S11. Current density versus scan rate for evaluating C_{dl} of (a) CoO NS, Co-B NS, Co-B-P NS, (b) Co-B-P NS, CoB/Co_2P HNA, (c) Co-B NS, Co-B HNA, and (d) the corresponding calculated ECSA values comparison.

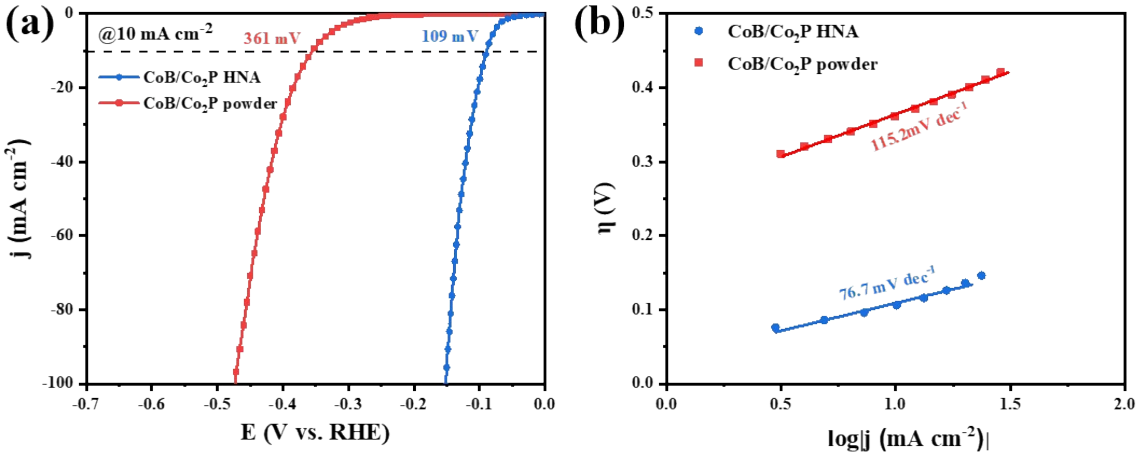

Figure S12. (a) LSV curves (b) corresponding Tafel plots of CoB/Co_2P powder and CoB/Co_2P HNA.

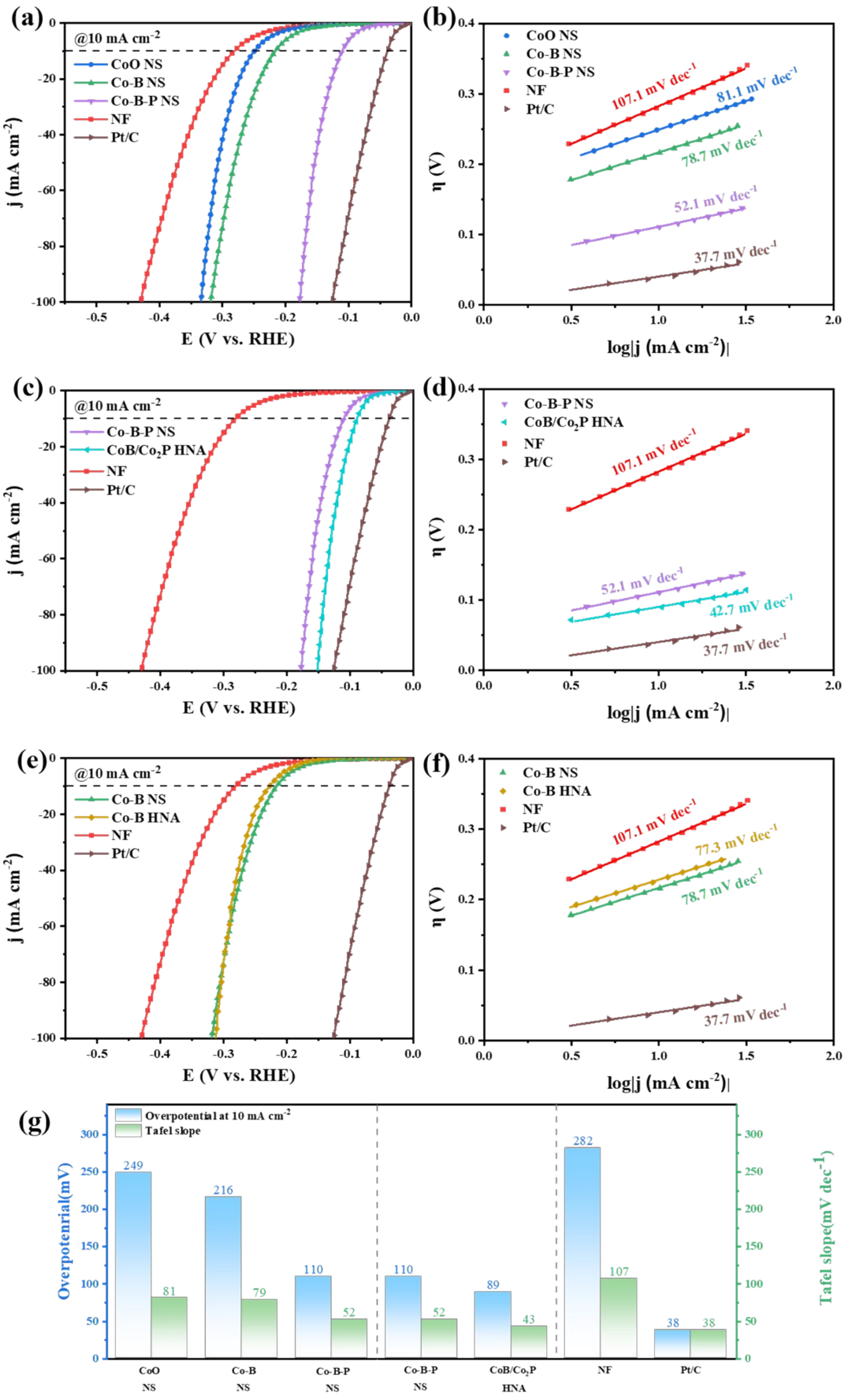

Figure S13. (a) LSV curves (b) corresponding Tafel plots CoO NS, Co-B NS, Co-B-P NS, NF and Pt/C, (c) LSV curves (d) corresponding Tafel plots of Co-B-P NS, CoB/Co_2P HNA, NF and Pt/C, (e) LSV curves (f) corresponding Tafel plots of Co-B NS NS, Co-B NS HNA, NF and Pt/C, (g) Tafel plots and overpotential at 10 mA cm^{-2} comparisons of above electrocatalysts. LSV and Tafel plots above are obtained after applying iR compensation to eliminate the effect of solution resistance.

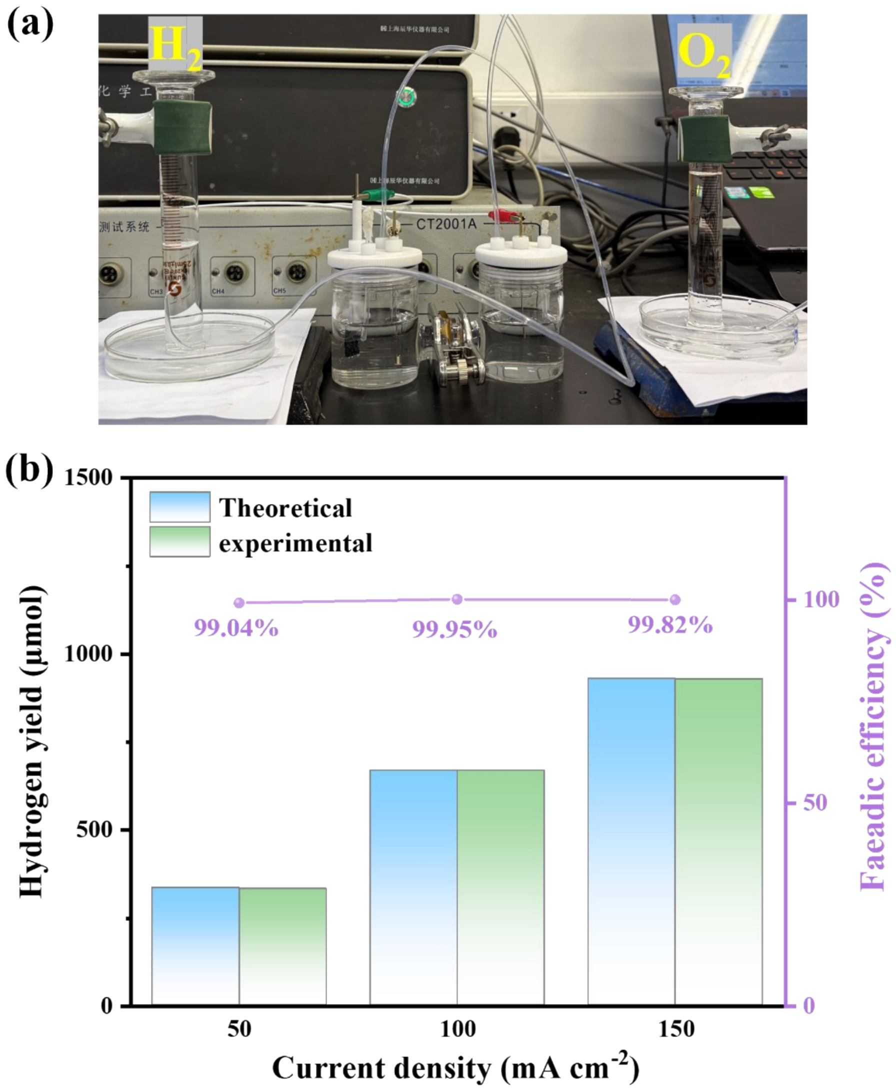

Figure S14. (a) Photo of water-splitting in H-cell, with the hydrogen-collection (drainage) setup used for gas evolution from the cathode during electrolysis (left) and the corresponding anode for oxygen (right), (b) the Faradaic efficiency (FE) of H_2 at different current density.

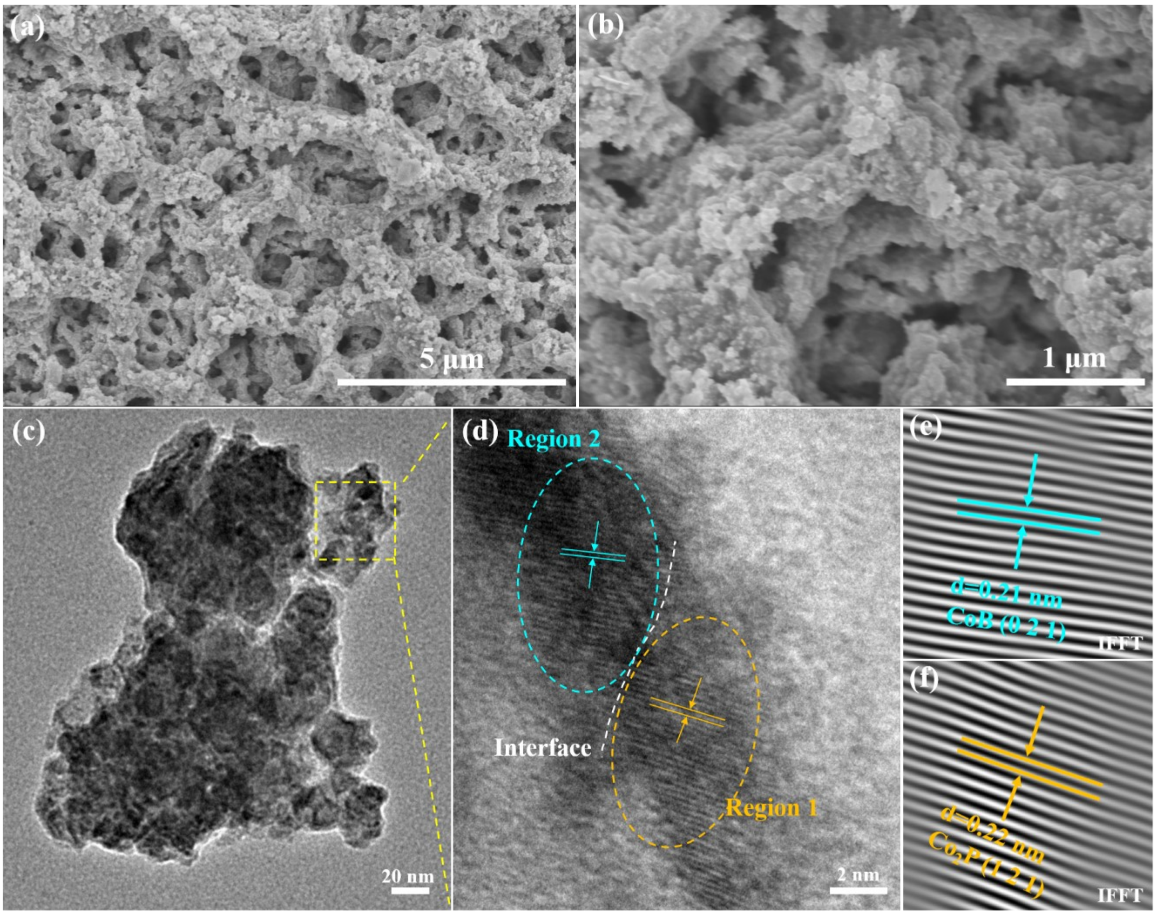

Figure S15. (a-b) Low- and high-magnification SEM images of post-HER CoB/Co_2P HNA, (c) TEM image (d) HRTEM image of post-HER CoB/Co_2P HNA, (e-f) IFFT of region 1 and region 2 in Figure S13d.

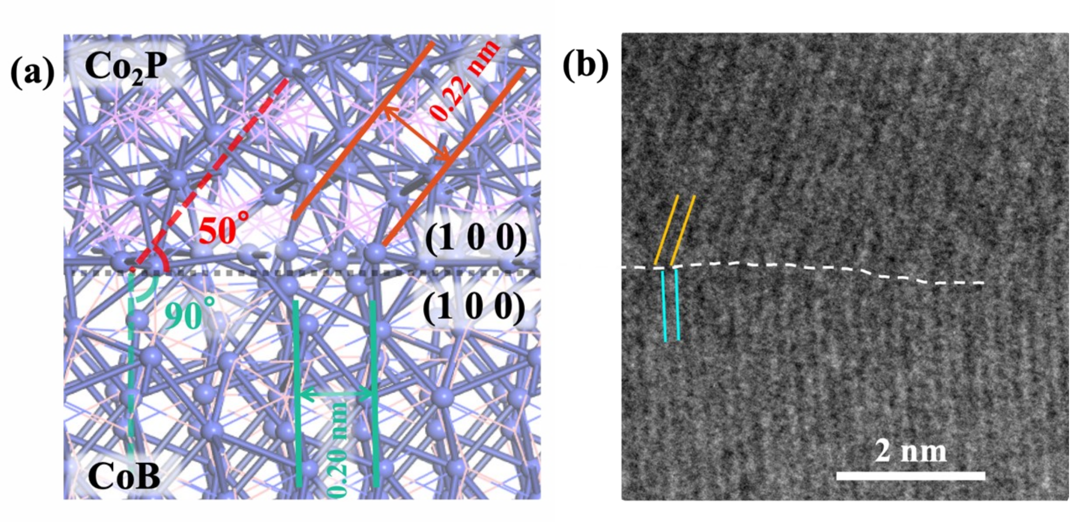

Figure S16. (a)The optimized structure of CoB(100)/Co_2P(100) interface, (b) HRTEM image of CoB/Co_2P HNA.

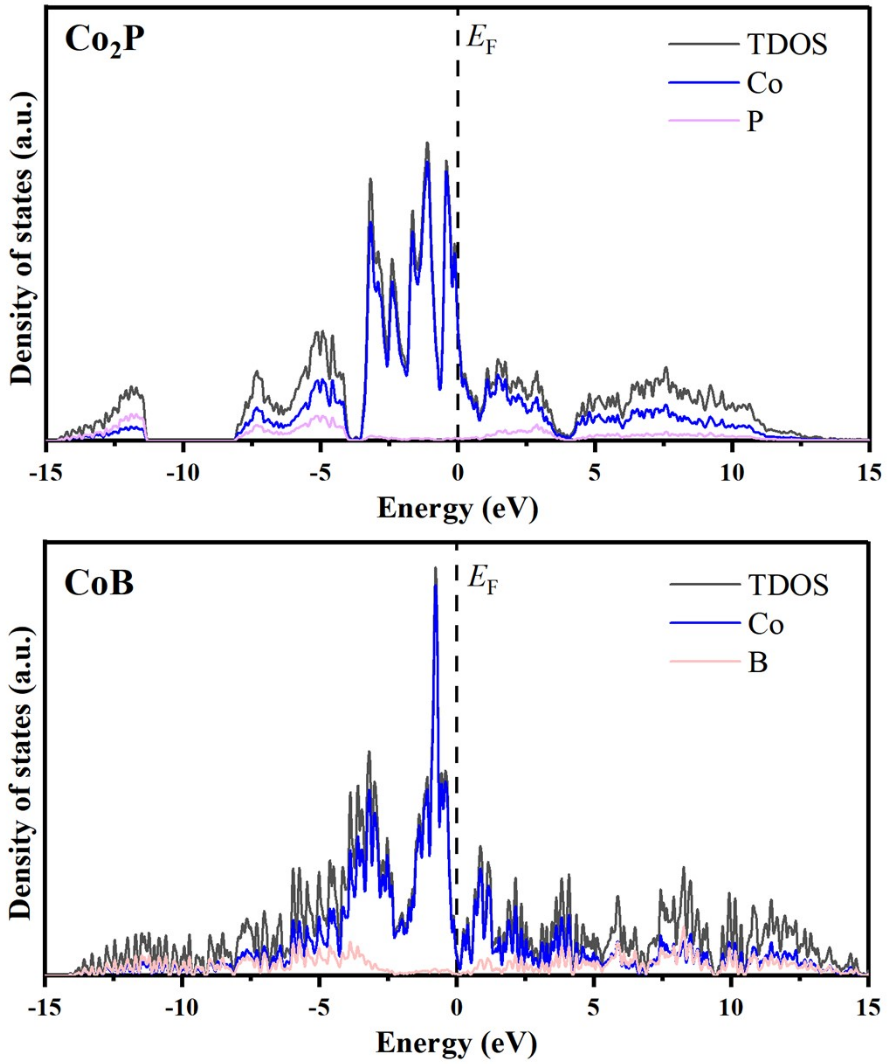

Figure S17. Total density of states of bulk Co_2P and CoB, and projected density of states of different elements in them.

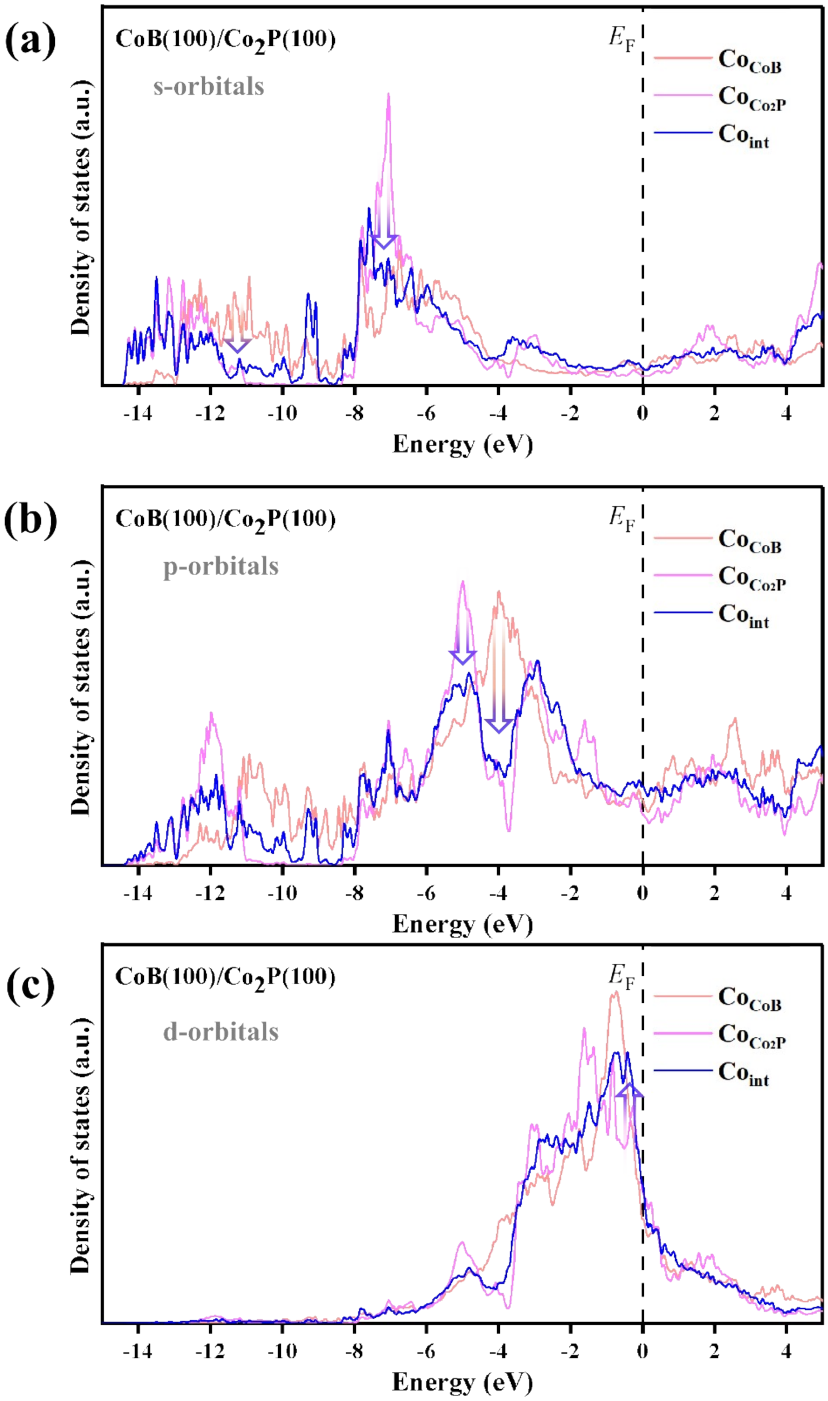

Figure S18. (a) Projected density of states of s-orbital of Co at different sites, i.e. Co atoms at interface sites (Co_{int}), Co at the CoB side (Co_{CoB}) and Co_2P side (Co_{Co_2P}). (b) Projected density of states of p-orbital of Co at different sites. (c) Projected density of states of d-orbital of Co at different sites.

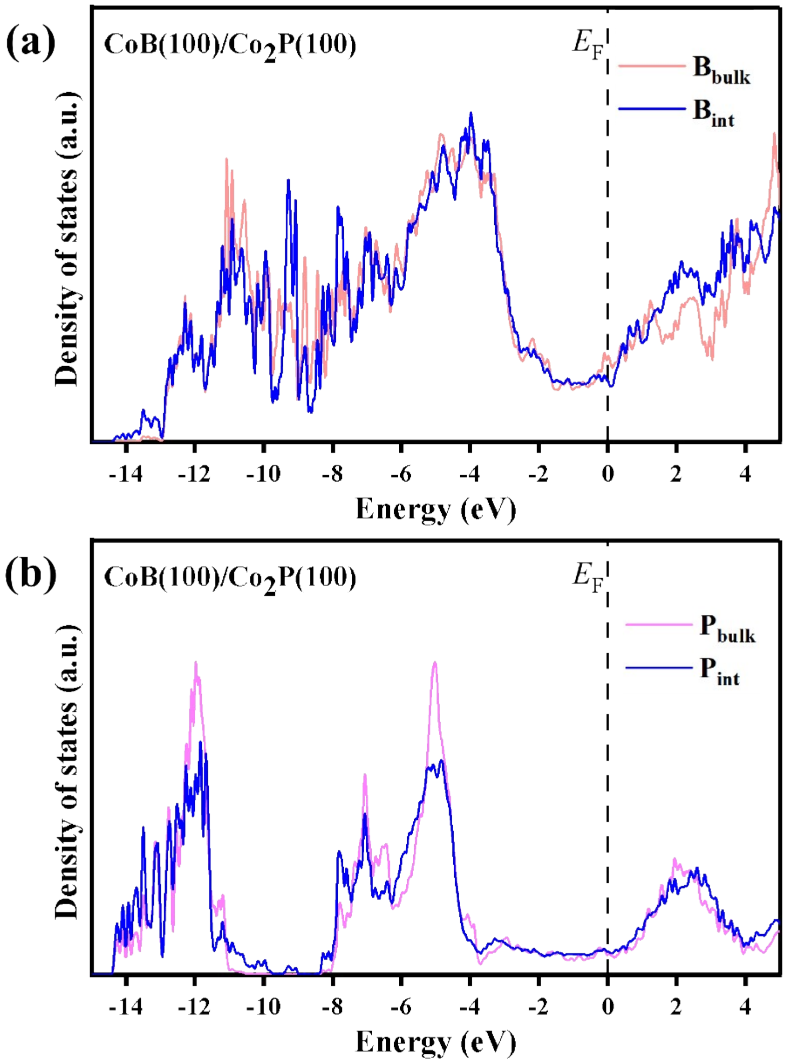

Figure S19. (a) Projected density of states of P at different sites, i.e. P atoms at interface sites (P_{int}), P at the bulk sites (P_{bulk}). (b) Projected density of states of B at different sites, i.e. B atoms at interface sites (B_{int}), B at the bulk sites (B_{bulk}).

Table S1. The mass loading of catalysts on the NF.

Catalysts	**Weight (g)**	**Mass loading on NF (mg)**	**Mass loading per geometric area (mg/cm^2)**
Cleaned NF	0.2202	/	/
CoO NS	0.2463	26.1	2.18
ZIF-67 precursor	0.2667	46.5	3.88
Co-B HNA	0.2565	36.3	3.03
CoB/Co_2P HNA	0.2681	47.9	3.99

Table S2. Elemental composition of CoB/Co_2P HNA determined by EDS.

Element	**Wt (%)**	**At (%)**
B K	2.17	4.02
C K	21.32	35.53
N K	1.04	1.49
O K	27.94	34.96
P K	25.59	16.54
Co L	14.64	4.97
Ni L	7.30	2.49

Table S3. Elemental composition (in At%) of CoB/Co_2P HNA and post-HER CoB/Co_2P HNA determined by XPS.

Element	**Pristine At%**	**Post-HER At%**
B	11.58	6.05
C	39.44	36.29
N	5.31	4.63
O	29.11	35.69
P	7.12	3.79
Co	3.28	5.88

Ni	4.15	7.68

Table S4. Performance comparison of this work and other HER catalysts.

Catalysts	η(mV) @10 mA cm^{-2}	Tafel slope (mV dec^{-1})	Electrolyte	Reference
CoB/Co_2P HNA (After IR correction)	**89**	**43**	**1 M KOH**	**This work**
Co/NBC-900	117	146	1 M KOH	[2]
Co-Ni-B/RGO	131	86	1 M KOH	[3]
B-CoO/Co@NC/NF	196	133	1 M KOH	[4]
Co-S-B-8	144	83	1 M KOH	[5]
CoP/CN@MoS_2	149	88	1 M KOH	[6]
CoMoP@N	179	144	1 M KOH	[7]
Co-P-O@CC	190	92	1 M NaOH	[8]
Co-S-P/CC	167	86	1 M KOH	[9]
CoP@N,P-C	113	98	1 M KOH	[10]
Co_1-Fe_1-B-P nanochains	173	96	1 M KOH	[11]
Co-P-B Electrode	172	68	0.5 M H_2SO_4	[12]
Co–Ni–B–P	192	94	1 M KOH	[13]
Co–B–P/g-C_3N_4	174	41	1 M KOH	[14]
Co-P-B	126	78	Alkaline simulated seawater	[15]

Section S4. References

[1] Kresse, G.; Furthmuller, J. Efficiency of ab-initio total energy calculations for metals and semiconductors using a plane-wave basis set. *Computational Materials Science* 1996, *6*, 15-50. DOI: 10.1016/0927-0256(96)00008-0

[2] Liu, M. R.; Hong, Q. L.; Li, Q. H.; et al. Cobalt boron imidazolate framework derived cobalt nanoparticles encapsulated in B/N codoped nanocarbon as efficient bifunctional electrocatalysts for overall water splitting. *Advanced Functional Materials* 2018, *28*(26), 1801136. DOI: 10.1002/adfm.201801136

[3] Jiang, L.; Wang, R.; Xiang, Z.; et al. Construction of Co-Ni-B heteronanosheets electrocatalyst for enhanced oxygen and hydrogen evolution. *International Journal of Hydrogen Energy* 2024, *51*, 898-906. DOI: 10.1016/j.ijhydene.2023.11.174

[4] Cha, D. C.; Singh, T. I.; Maibam, A.; et al. Metal-organic framework-derived mesoporous B-doped CoO/Co@N-doped carbon hybrid 3D heterostructured interfaces with modulated cobalt oxidation states for alkaline water splitting. *Small* 2023, *19*(35), 2301405. DOI: 10.1002/smll.202301405

[5] Suryawanshi, A.; John, R. A. B.; Bhide, A.; et al. Designing bifunctional electrocatalysts based on complex cobalt-sulfo-boride compound for high-current-density alkaline water electrolysis. *Energy & Fuels* 2024, *38*(19), 18965-18975. DOI: 10.1021/acs.energyfuels.4c02350

[6] Li, J. G.; Xie, K.; Sun, H.; et al. Template-directed bifunctional dodecahedral CoP/CN@MoS_2 electrocatalyst for high efficient water splitting. *ACS Applied Materials & Interfaces* 2019, *11*(40), 36649-36657. DOI: 10.1021/acsami.9b12199

[7] Sun, D.; Lin, S.; Yu, Y.; et al. One-pot synthesis of N and P co-doped carbon layer stabilized cobalt-doped MoP 3D porous structure for enhanced overall water splitting. *Journal of Alloys and Compounds* 2022, *895*, 162595. DOI: 10.1016/j.jallcom.2021.162595

[8] Sharma, P. J.; Siraj, S.; Sahatiya, P.; et al. Electroless plating of Co-P-O electrocatalyst on carbon cloth for alkaline water electrolysis. *Journal of Electroanalytical Chemistry* 2024, *967*, 118491. DOI: 10.1016/j.jelechem.2024.118491

[9] Sheng, S.; Ye, K.; Sha, L.; et al. Rational design of Co-S-P nanosheet arrays as bifunctional

electrocatalysts for both ethanol oxidation reaction and hydrogen evolution reaction. *Inorganic Chemistry Frontiers* 2020, *7*(22), 4498-4506. DOI: 10.1039/D0QI00977J

[10] Sun, D.; Lin, S.; Yu, Y.; et al. In-situ phosphating Co@Nitrogen-doping graphene boosts overall water splitting under alkaline condition. *Journal of Electroanalytical Chemistry* 2022, *904*, 115882. DOI: 10.1016/j.jelechem.2021.115882

[11] Wu, Z.; Nie, D.; Song, M.; et al. Facile synthesis of Co–Fe–B–P nanochains as an efficient bifunctional electrocatalyst for overall water-splitting. *Nanoscale* 2019, *11*(15), 7506-7512. DOI: 10.1039/C9NR01151F

[12] Kim, J.; Kim, H.; Kim, S. K.; et al. Electrodeposited amorphous Co–P–B ternary catalyst for hydrogen evolution reaction. *Journal of Materials Chemistry A* 2018, *6*(15), 6282-6288. DOI: 10.1039/C8TA00972A

[13] Dong, D.; Xu, X.; Ma, C.; et al. Partial phosphorization of porous Co–Ni–B for efficient hydrogen evolution electrocatalysis. *International Journal of Hydrogen Energy* 2020, *45*(7), 4545-4555. DOI: 10.1016/j.ijhydene.2019.12.124

[14] He, Q.; Wang, L.; Xiao, F.; et al. Cauliflower-like Co–B–P ternary catalyst loaded on graphitic carbon nitride nanosheets with synergistically enhanced electrocatalytic activity for hydrogen evolution reaction. *International Journal of Hydrogen Energy* 2024, *58*, 149-157. DOI: 10.1016/j.ijhydene.2024.01.046

[15] Silviya, R.; Bhide, A.; Gupta, S.; et al. Bifunctional amorphous transition-metal phospho-boride electrocatalysts for selective alkaline seawater splitting at a current density of 2A cm^{-2}. *Small Methods* 2024, *8*(8), 2301395. DOI: 10.1002/smtd.202301395